

RSC Advances



This is an *Accepted Manuscript*, which has been through the Royal Society of Chemistry peer review process and has been accepted for publication.

Accepted Manuscripts are published online shortly after acceptance, before technical editing, formatting and proof reading. Using this free service, authors can make their results available to the community, in citable form, before we publish the edited article. This *Accepted Manuscript* will be replaced by the edited, formatted and paginated article as soon as this is available.

You can find more information about *Accepted Manuscripts* in the [Information for Authors](#).

Please note that technical editing may introduce minor changes to the text and/or graphics, which may alter content. The journal's standard [Terms & Conditions](#) and the [Ethical guidelines](#) still apply. In no event shall the Royal Society of Chemistry be held responsible for any errors or omissions in this *Accepted Manuscript* or any consequences arising from the use of any information it contains.

White clovers based nitrogen-doped porous carbons for a high energy density supercapacitor electrode

Guofu Ma^{a*}, Zhiguo Zhang^a, Kanjun Sun^b, Hui Peng^a, Qian Yang^a, Feitian Ran^a and Ziqiang Lei^{a*}

^aKey Laboratory of Eco-Environment-Related Polymer Materials of Ministry of Education, Key Laboratory of Polymer Materials of Gansu Province, College of Chemistry and Chemical Engineering, Northwest Normal University, Lanzhou 730070, China.

^bCollege of Chemistry and Environmental Science, Lanzhou City University, Lanzhou 730070, China.

E-mail: magf@nwnu.edu.cn, leizq@nwnu.edu.cn

ABSTRACT: We have employed the biomaterial white clovers as carbon precursor and ZnCl₂ as activating agent to prepare white clovers carbons (WCCs). The WCC-2 (mass ratios of white clovers and ZnCl₂ is 1:2) possesses as high as 6.9 wt% nitrogen content and 857 m² g⁻¹ BET surface area. Furthermore, it exhibits 233.1 F g⁻¹ specific capacitance at the current density of 1.0 A g⁻¹, even 82.9% capacitance retention at 20 A g⁻¹ in 2 mol L⁻¹ KOH electrolyte. The specific capacitance could remain at almost about 100.0% when the cycle number is between the 200-5000 cycles. Because of the wide potential window (0-2.0 V) and high specific capacitance, the WCC-2//WCC-2 symmetric capacitor shows an energy density of 30-13.1 Wh kg⁻¹ under the power outputs of 503.5-9991.5 W kg⁻¹ in 0.5 mol L⁻¹ Na₂SO₄ electrolyte. The results demonstrate WCC-2 can be a promising candidate for the electrode material of high performance supercapacitors.

KEYWORDS: Supercapacitor; High energy density; Nitrogen-doped carbon; White clovers

1. Introduction

Supercapacitor is perfectly adapting for the quality of electricity required by energy efficient industrial equipment, electric and hybrid electric vehicles and smart-grid applications, for it has high power density and good cyclability. Although, the energy density of supercapacitors is several orders of magnitude higher than that of conventional capacitors, but compared with batteries (e.g., lithium-ion batteries), the energy density is low. [1] Therefore, in the development of supercapacitor, the most critical aspect is to provide higher energy density while maintaining power density and cyclability.

To meet such demands, porous carbon materials are paid more attention as electrode materials for supercapacitor because of their controllable pore size, high surface area, high thermal stability, low cost and good corrosion resistance. [2] The carbon electrode is primarily made up of the electrical double layer capacitors (EDLC), which are based on electrostatic attraction to generate charge accumulation and formed at the electrode/electrolyte interface.[3, 4] To develop high performance carbon electrode, and further enhance the energy density of supercapacitor, it is crucial to understand the capacitive performances of porous carbons depend on not only pore structures but also surface functionality of carbon. [5, 6] In this respect, one approach is to introduce abundant porous structure and incorporate heteroatoms into carbon frameworks. [7-9] The incorporation of heteroatoms, especially nitrogen, into carbon materials can improve the specific capacitance considerably, because the nitrogen-containing functional groups can improve the wettability of carbon materials to electrolyte solution, enhance the electronic conductivity while maintaining the superb cycle ability. [10, 11] A variety of nitrogen-doped porous carbon have been developed to meet this challenge, which is usually prepared by treating porous carbon with urea, amines, or ammonia, [12, 13] or using various nitrogen-containing carbon precursors with synthetic polymers, [14, 15] and ionic liquids [16, 17]. However, the

preparation processes for these carbons require expensive and non-renewable raw materials, a lot of time and energy, and tedious preparation procedures.

Recent advances in electrode materials, such as, biomass or biomass derivatives offer significant opportunities to develop new, improved electrode materials from renewable resources. Wang et al. prepared microporous chicken feather carbon via the activation with KOH agent, which exhibits the highest initial specific capacitance of 302 F g^{-1} at current density of 1 A g^{-1} in $1 \text{ M H}_2\text{SO}_4$. [18] Ding et al. created a high performance hybrid sodium ion capacitor with the active materials in both anode and the cathode being approximately balanced in their capacity and derived entirely from biomass waste peanut shells. [19] And Wu et al. used the watermelon as carbon source to prepare sponge-like carbonaceous hydrogels and aerogels through a novel, eco-friendly hydrothermal carbonization method. [20]

It is well known that the white clovers (*Trifolium repens*) grow all over the world, which are very cheap, easily available and drought tolerance. In general, white clovers work well as a major forage legume of considerable economic importance in temperate agricultural systems because of abundant nutrition. [21] Furthermore, it is a potential raw material to prepare nitrogen-doped porous carbons with good electrochemical capacitive performance because white clovers can fix nitrogen. [22] As a result of all these inherent advantages, white clovers are generating very strong interest with regard to be biomass carbon materials for supercapacitors.

2 Experimental

2.1 Materials

White clovers (*Trifolium repens*) derived from the local environment (Lanzhou Gansu province, China), zinc chloride (ZnCl_2 , Yantai Shuangshuang Chemical Co., Ltd, China). All chemical reagents were in analytical grade.

2.2 Preparation of nitrogen-doped porous carbon based on white clovers

Before carbonization, the raw materials (white clovers) were physically mixed with ZnCl_2 in the variable mass ratios of 1:1, 1:2 and 1:3, respectively. It has been proven that physical mixing was chosen as the contacting method because in most cases it can lead to better porosity development than impregnation. [23] The graphitization, activation and nitrogen-doped process of the white clovers were simultaneously carried out in a tubular furnace by heating up to $700\text{ }^\circ\text{C}$ under a N_2 flow with a heating rate of $5\text{ }^\circ\text{C min}^{-1}$, and further holded $700\text{ }^\circ\text{C}$ for 2 h. Furthermore, the raw materials were carried out under the same conditions for comparison purposes. All samples were thoroughly washed several times with 2.0 mol L^{-1} HCl to remove inorganic salts and any unwanted impurities, and then with distilled water until neutral pH was achieved. Finally, the carbon samples were dried in an oven at $60\text{ }^\circ\text{C}$ for 24 h. Hereafter, we name the as-prepared carbons with the different mass ratio of the white clovers and activating agent (1:0, 1:1, 1:2 and 1:3) as WCC-0, WCC-1, WCC-2 and WCC-3, respectively.

2.3 Characterization of various carbon materials

The morphologies of the carbons were characterized using the field emission scanning electron microscopy (FE-SEM, Ultra Plus, Carl Zeiss) at an accelerating voltage of 5.0 kV. The structure of the samples was characterized by a transmission electron microscopy (TEM, JEM-2010 Japan). X-ray diffraction (XRD) of samples was obtained on a Rigaku D/Max-2400 diffractometer with $\text{Cu K}\alpha$ radiation ($k = 1.5418\text{ \AA}$) at 40 kV, 100 mA and the 2θ range from 5° to 80° . Raman spectra was evaluated at ambient temperature through an in Via Raman spectrometer (Renishaw) with an Argon ion laser ($\lambda = 514\text{ nm}$). The Brunauer-Emmett-Teller surface area (S_{BET}) and pore structure of the carbon samples were analyzed by nitrogen adsorption in a Micromeritics ASAP 2020 nitrogen adsorption apparatus (U.S.A.), and all samples were degassed at $200\text{ }^\circ\text{C}$ prior to nitrogen adsorption measurements. The elemental microanalysis (C, H and N) was carried out using the Elemental Analyzer Vario EL and X-ray photoelectron spectroscopy (XPS) measurement was performed on an

Escalab 210 system (Germany).

2.4 Electrochemical measurements

Cyclic voltammetry (CV) studies of the all carbons were performed with an electrochemical workstation (CHI 660D) in a three-electrode system. The glassy carbon electrode with a diameter of 5 mm was employed as the working electrode, high purity carbon rod as the counter electrode, and Hg/HgO (1 mol L⁻¹ KOH) as the reference electrode. Typically, 4 mg as-prepared products with assistance by ultrasonic vibration dispersed in 0.4 mL of 0.25 wt% Nafion (DuPont, USA) ethanol solutions. Then, 8 μ L above suspension was dropped onto the glassy carbon electrode and dried for 10 minutes at room temperature. Electrochemical impedance spectroscopy (EIS) measurements was performed in the frequency between 0.1 Hz and 100 kHz and impedance amplitude of ± 5 mV at an open circuit potential. The cycle-life stability was obtained on the cycling testing equipment (CT2001A, Wuhan Land Electronic Co. Ltd., China).

Besides, the capacitive performance of WCC-2 was investigated using a two-electrode testing cell. The working electrode was prepared by uniformly stirring the WCC-2 power into the mixture of polyvinylidene fluoride (PVDF) and commercial carbon black in N-methyl-2-pyrrolidone (NMP) until formed a homogeneous slurry. The slurry was coated on nickel foam and dried at 80 °C for 12 h, then weighted and pressed it into sheets under 10 MPa. The total mass was close to 4 mg of each electrode as a device for the measurements. Two as-prepared WCC-2 electrodes are fabricated with the separator (thin polypropylene film) and electrolyte solution (0.5 mol L⁻¹ Na₂SO₄ aqueous solutions) symmetrically into a sandwich-type cells construction (electrode/separator/electrode).

3. Results and Discussion

3.1 Morphologies and chemical features of activated carbons

The morphology and high porosity of the white clovers and carbon samples are investigated by FE-SEM

techniques (Figure 1). The internal structure of the white clover is shown in Figure 1a and lots of irregular pores in the macroscopic scale and rough surface could be observed. However, after carbonization, it is obviously seen from Figure 1b that the WCC-0 has a smooth surface and the pristine macropores disappeared, which might be due to the collapse of the pores in the process of heating-up. The activated carbon materials seem to be accumulated by small carbon spherical particle, which might make ionic diffusion from bulk electrolyte into the inner space of carbon materials easily. By contrast, the size of the carbon particles of WCC-2 is smaller than WCC-1. And WCC-2 (Figure 1d) looks composed of small carbon fragments and also more loose and less agglomeration than WCC-1 (Figure 1c). Being different from others, there generated macropores and carbon layer which accumulated randomly in the WCC-3 (Figure 1e).

In addition, the TEM image in Figure 2a demonstrate that the WCC-2 has a well-defined pore system consisting of abundant inherent and disordered three-dimensional mesopore porous structure which is beneficial to the fast diffusion of electrolyte ions from bulk electrolyte into the inner space of carbon materials. High resolution TEM images clearly exhibit a highly developed microporous structure due to carbonization and the activation of the white clovers. Notably, this kind of micro-mesopores structure is very important to have rapid charge/discharge at large current densities and excellent rate capability performance, because of the micropores can provide high specific surface areas to store charges meanwhile the interconnected mesopores can make diffusion and transport of electrolyte easier. [24]

In order to investigate the development of porosity by ZnCl_2 activation, the specific surface areas and pore structures of the activated carbon samples were measured by N_2 adsorption-desorption technique. As given in Figure 3a, it is clear that WCC-0 prepared without activating agent shows a type I absorption isotherm (according to the IUPAC classification) indicating the non-porous characteristic. But with the increase of the white clovers/ ZnCl_2 mass ratio, the dramatically increased adsorption volumes show a much more developed

porous structure, while the wider knee at lower relative pressure indicates wider pores, proving the white clovers/ZnCl₂ mass ratio might be an important factor for controlling the development of porosity by ZnCl₂ chemical activation. Specifically, the carbons after activation display between type II and type IV adsorption isotherms with a much higher N₂ adsorption capacity than WCC-0 indicating the abundant pore structure. In addition, the isotherms of the activated carbon samples (WCC-1, WCC-2 and WCC-3) are assigned to the typical type H-4 hysteresis loops at the relative pressure from 0.40 to 1.0 implying the coexistence of mesopores, which are associated with aggregates of plate-like particles giving rise to slit-shaped pores. And the sharp increase in adsorption capacity for the activated carbon samples at low relative pressure ($P/P_0 < 0.2$) could be attributed to the strong adsorption of N₂ in micropores. Furthermore, the obvious tails at higher relative pressures approaching to 1.0 demonstrate the existence of macropores. [25] These results indicate that the samples include not only predominant mesopores but also a certain amount of micropores and macropores.

The pore structure is also confirmed by the pore size distribution plots, which is recorded from the adsorption branch of the isotherm based on BJH model (Figure 3b) and associated with non-local density functional theory (the inset of the Figure 3b). As shown in Figure 3b and the inset, the activated carbons have well-developed porous structure and exhibit much more pores with diameters centered in the microporous and mesoporous regions than WCC-0. As a result, the more activating agent added, the larger porosity of the carbon generated by chemical activation. [26, 27] It is possible that while ZnCl₂ corroded, the micropores were formed and the mesopore of WCC were expanded at high temperature of 700°C. However, in the pore diameter range of 2-100 nm, apparent differences can be found with WCC-2 and WCC-3 as compared with WCC-1 which has an obviously lower intensity in mesopores and macropores. It also can be seen that WCC-3 possesses somewhat more mesopores and macropores than WCC-2. In more detail, the plots (the inset of the Figure 3b) indicate that the porosity of the activated carbons mostly consist of wider pores distribution in well-defined pore systems:

micropores (0.3 nm, 0.6-2 nm) and smaller mesopores (2-5 nm). And the WCC-2 contains multi-level micropores centered at 0.6 nm and 1.2 nm which provide the hierarchical microstructure to store and insert the electron efficiently and ensure the electron access to those sites. [24]

Apart from the above mentioned analysis, Table 1 containing BET specific surface areas and pore volumes can provide the textural properties of the carbon samples more precisely. The activated porous carbon materials show much higher specific surface area and pore volume than the directly carbonized the white clovers (Figure 3a, Table 1), indicating the high efficiency of ZnCl_2 activating agent on pore propagation and widening at the same time. Accordingly, the as-prepared carbons after activation contain abundant both mesopores and micropores. Even though the nitrogen adsorption-desorption isotherms and BET specific surface areas of WCC-2 and WCC-3 are very similar, there are obvious differences about the micropores volumes and the average pore diameter. That is, the BET specific surface areas of WCC-2 and WCC-3 are 857.0 and 851.0 $\text{m}^2 \text{g}^{-1}$, but their micropores areas are 194.6 and 121.3 $\text{m}^2 \text{g}^{-1}$, their average pore widths are 3.71 and 4.02nm, which demonstrates there are more abundant micropores and less mesopores and macropores in the WCC-2 than WCC-3. This fact is identical with the results of Figure 3b. The pore structure in WCC-2 is believed to be more beneficial for supercapacitor, because the actual energy storage takes place predominately in the micropores, meanwhile, the larger pores can provide fast mass-transport of electrolytes. [3]

Elemental analysis were employed on all nitrogen-doped porous carbons based on white clovers because the chemical activation can also influence the nitrogen content. As listed in Table 1, the nitrogen contents of WCC-0, WCC-1, WCC-2 and WCC-3 are 4.1, 6.8, 6.9, and 6.8 wt%, respectively, which increase after activation and almost keep stable whatever the mass ratio of the raw material to the activation agent is at 700°C. This result indicates there might retain the nitrogen content of the carbons during the activation and carbonization.

The X-ray photoelectron spectroscopy (XPS) analysis was used to further investigate the surface nitrogen chemical composition in WCC-2. Figure 4a demonstrates a predominant C 1s peak at around 299.8 eV, a weak O 1s peak near 544.8 eV, and a pronounced N 1s peak located at about 413.8 eV, with atomic concentrations of 87.78, 5.85, and 5.37%, respectively. The N 1s peak further confirms the doping of N atoms in the carbon frame, which can produce defects in carbon as well as improve the hydrophilicity, increase the utilization ratio of surface area and additional active sites for supercapacitor. [28, 29] The binding energy peaks observed in the high-resolution N 1s profile (Figure 4b) can be basically deconvoluted into four peaks located at 398.5, 400.1, 401.4, and 403.7 eV, which are attributed to pyridinic (N-6), pyrrolic and pyridone (N-5), quaternary (N-Q), and pyridine-N-oxide(N-X) groups, respectively. [30] The surface nitrogen species include N-6 (37.3 %), N-5, (28.6 %), N-Q (17.0 %) and N-X (17.1 %), and the N-6 and N-5 species content are as high as 65.9% of the total nitrogen atoms of WCC-2, which are considered to improve the performance of the supercapacitors. [31] In addition, to analyze the elemental distribution, the WCC-2 was further characterized by element mapping images of carbon, oxygen and nitrogen (Figure 4c). The uniform distribution of blue dots (nitrogen) suggests that nitrogen is uniformly doped in WCC-2 skeleton.

X-ray diffraction (XRD) analysis was used to investigate the structure of WCC-2. As seen from Figure 5a, two typical peaks can be observed. The clear observation of (002) diffraction peak at around $2\theta = 23.7^\circ$ indicating that the activated carbon consists of small domains of ordered graphene sheets, and another diffraction peak centered at $2\theta = 42.5^\circ$ which can be approximately indexed as (100) plane of standard graphite. Notably, both diffraction peaks are broad in width and low intensity in height, suggesting the amorphous feature of the WCC-2 with partial graphitization.

Raman spectroscopy analysis was employed to further investigate the structure of the WCC-2 sample. As given in Figure 5b, the peaks at 1346 and 1600 cm^{-1} represent the D band and the G band of carbon material,

respectively, which are characteristic Raman peaks for carbon materials. [32] As is known, the D band is generally associated with A_{1g} symmetry which corresponds to the disordered carbon or defective graphitic structures, whereas the G band is characteristic feature of the graphitic layers due to the E_{2g} phonon of sp^2 carbon atoms corresponding to the tangential vibration of the carbon atoms. [33] In addition, the relative intensity ratio of the D to G band (I_D/I_G) is proportional to the number of defect sites of carbon and used to examine the degree of disorder in the graphitic structure. That is, the higher the ratio, the lower the degree of graphitization. For WCC-2, the I_D/I_G ratio was 0.95, indicating partially graphitized and a relatively lower degree of graphitization than that of the commercial activated carbon (0.52). [34] These observations from XRD and Raman analysis further suggest that the WCC-2 possesses a partial graphitization structure, which might lead to its good electronic conductivity.

3.2 Electrochemical characterization of activated carbons

The obtained carbons were used as electrode materials of supercapacitor, and their electrochemical behaviors have been analyzed in 2 mol L^{-1} KOH electrolyte employing a standard three-electrode system within a voltage window of -1.0-0 V. Obviously, from the Figure 6a, the WCC-0 shows a triangle CV curves shape while the activated carbons exhibit quasi-rectangular CV curves at the scanning rates of 50 mV s^{-1} . As is known, the larger for the area of CV curve, the higher for the capacitance of electrode. [35] Comparatively, the CV curve area of WCC-2 is much higher than that of others, displaying a higher specific capacitance.

Galvanostatic charge/discharge has also been employed to estimate the electrochemical performance of all carbon samples as electrode materials for supercapacitor at the density of 1 A g^{-1} . It can be clearly seen in the Figure 6b that the shapes of all GCD curves are linear and symmetrical, suggesting that the electrodes possess an ideal capacitive performance and splendid electrochemical reversibility. The WCC-2 sample still maintains the appearance of roughly rectangular-like shapes at high scan rate, even up to 200 mV s^{-1} , indicating an ideal

electrochemical capacitive behavior with rapid diffusion and easy transportation of electrolyte ions to the interface of the electrode (Figure 6c). It might be due to synergistic effect of porous structure in WCC-2 which promotes ion diffusion and electrolyte/electrode wettability.

Figure 6d shows the GCD curves of WCC-2 at different current densities (0.5-20 A g⁻¹). It is clear that the shapes of the charge/discharge curves are closely linear and symmetrical, indicating an excellent capacitive behavior and electrochemical reversibility. Even when the current density increases to 20 A g⁻¹, the galvanostatic charge/discharge curves still remain a nearly linear-like shape. In addition, specific capacitances of the electrode at different densities are calculated according to the equation: $C_s = I\Delta t/(m\Delta V)$, in which I is the discharge current, Δt is the discharge time from 0 to -1 V, ΔV is the voltage difference within the discharge time, and m represents the mass of carbon on an electrode. Furthermore, it can be obtained from the Figure 6e that the WCC-2 electrode exhibits a specific capacity ranging from 233.1 F g⁻¹ at 1 A g⁻¹, to 193.2 F g⁻¹ at 20 A g⁻¹. That is, the WCC-2 electrode can remain 82.9% of initial specific capacitance with current densities changing from 1 to 20 A g⁻¹, indicating that the activated carbon electrode possesses good capacitance retention capability. When the current density is no less than 10 A g⁻¹, the specific capacitance does not change obviously, and tends to be stable.

Electrochemical impedance spectroscopy (EIS) is used to investigate the facilitated ion- or electron-transport kinetics within the WCC-2 electrodes. Figure 6f displays the Nyquist plot of WCC-2 electrode in 2 mol L⁻¹ KOH at the frequency range 0.1 Hz to 100 kHz. It is composed of three distinct parts at different frequency range, including an uncompleted semicircle part at high frequency, a inclined portion of the curve (about 45°) at middle frequency and a linear part at low frequency. At high frequency region (the inset of Figure 6f), the intercept at real axis gives the internal resistance value of the cell capacitor (R_s), which is the sum of ionic resistance of electrolyte, intrinsic active material resistance and the contact resistance at the interface of the

active material and the current collector. [36] The diameter of the semicircle reflects the charge transfer resistance (R_{ct}), which is related to the charge transfer through the electrode/electrolyte interface. A smaller semicircle means a lower charge-transfer resistance. The 45° slope of the line in the middle frequencies is ascribed to the Warburg impedance (W), responding to the frequency dependence of ion diffusion/transport from electrolyte to the pore surface of carbon electrode. The almost vertical line indicates the swift ion diffusion in electrolyte and ion adsorption onto the electrode surface and represents the dominance of ideal double-layer charge/discharge behaviors at low frequency. [37] The Nyquist plots are also fitted and interpreted with the help of an appropriate electric equivalent circuit (the inset of Figure 6f). The capacitor circuit consists of R_s , R_{ct} , W , C_L , C_{dl} and Q , in which C_{dl} and Q are related to the capacitor layer formed during the charge-discharge process, and C_L reflects the limit capacitance. [38] As it can be concluded, the WCC-2 not only has a low R_s ($3.5 \Omega \text{ cm}^2$), but also possesses a small R_{ct} ($0.97 \Omega \text{ cm}^2$), as well as owns a small Warburg resistance ($0.017 \Omega \text{ cm}^2$). These values indicate that the ion diffusion and electrolyte permeation into the pore structure is easier, which might facilitate the formation of the electric double layer. The result might be ascribed to partial graphitization, high surface area and controlled pore sizes as well as high nitrogen contents.

Figure 6g indicates the cycling stabilities of WCC-2 electrode investigated by GCD measurement at a current density of 1 A g^{-1} for 5000 cycles. It is clear that the specific capacitance still remains at almost about 100.0% of the capacitance value of the 200 cycles after 5000 cycles, and GC curves of the first three and the last three cycles are almost identical isosceles triangles (Figure 6g inset), which indicate that the WCC-2 delivers an excellent cycling stability as an electrode material for supercapacitors.

To further investigate the electrochemical performance of the WCC-2 electrode in a full cell set-up by cyclic voltammetry and galvanostatic charge/discharge test, a symmetric supercapacitor based on two equal WCC-2 is developed in a two-electrode system. According to the equation $E = 1/2CV^2$, the energy density is not only

related to the capacitance of the symmetric supercapacitor but also closely interrelated with the operating voltage. To further enhance the energy density of the symmetric capacitor, the strategy of improving the operation voltage is a vital candidate. One of the suitable methods is to select optimal electrolyte for the two-electrode symmetric supercapacitors. And the neutral Na_2SO_4 aqueous solution electrolyte stands out above the rest in the recent years, because the carbon//carbon symmetric capacitors possess a larger operation voltage Na_2SO_4 aqueous solution than in acid and alkali solutions. More importantly, it is cost-efficient, environmentally friendly, and easier to get than organic solution. [39] Therefore, the WCC-2//WCC-2 symmetric supercapacitor is fabricated in 0.5 mol L^{-1} Na_2SO_4 aqueous solution. Furthermore, due to the vital influence of the voltage range, CV curves in different ranges are performed to determine the stable and optimal voltage range. As shown in Figure 6a, it can be clearly seen that the operating cell voltage can be greatly extended. CV curves of the WCC-2//WCC-2 device are measured at 50 mV s^{-1} with different potential windows. It is obviously seen that all curves exhibit rectangular-like shapes (Figure 7a) and no obvious increase of anodic current even at the potential window up to 2.0 V, implying an ideal capacitive behavior and a fast charge/discharge property. Therefore, the detailed investigation of WCC-2//WCC-2 symmetric supercapacitor are performed in the voltage range of 0-2.0 V.

It is clear from Figure 7b that all curves of the WCC-2//WCC-2 symmetric capacitor display a quasi-rectangular shape, even at the scan rate as high as 150 mV s^{-1} , indicating a good charge propagation with an excellent rate capability and suggesting the characteristics of double-layer capacitance. This characteristic of the carbon material is associated with the porous feature that can be accessed freely and quickly by electrolyte ions. These results can be further confirmed by galvanostatic charge/discharge measurements. As shown in Fig. 7c, the GCD curves of the WCC-2//WCC-2 device exhibit nearly triangular shapes with a small deviation from linearity, implying excellent electrochemical reversibility and low internal series resistance. [40] In addition, the

WCC-2 capacitor delivers specific capacitances of 44.0 F g⁻¹ and 36.9 F g⁻¹ at the current density of 0.5 A g⁻¹ and 1.0 A g⁻¹, based on the total active material mass of two electrodes. Ragone plot in the Figure 7d shows the comparison of the power and energy densities of the WCC-2//WCC-2 symmetric capacitor device in 0.5 mol L⁻¹ Na₂SO₄ electrolyte. The specific energy density (E , Wh kg⁻¹) and power density (P , W kg⁻¹) for the supercapacitor cell can be calculated from the discharge curves at different current densities using the following equations:

$$E = 1/2CV^2 \quad (2)$$

$$P = E/t \quad (3)$$

where C is the specific capacitance of the supercapacitor cell, V is the voltage change, and t is the discharge time. Because of the wide potential window and high specific capacitance, the symmetric capacitor shows an energy density of 30-13.1 Wh kg⁻¹ under the power outputs of 503.5-9991.5 W kg⁻¹. The value of energy density of WCC-2//WCC-2 symmetric supercapacitor is much higher than those of the carbon-based aqueous symmetric supercapacitor previously reported, such as microporous chicken feather carbon (4.77 Wh kg⁻¹), [18] porous carbon layers (25.7 Wh kg⁻¹), [40] a porous carbon prepared by corncob residue (15 Wh kg⁻¹), [41] and three-dimensional hierarchically porous carbon prepared by the carbonization of polyaniline (10.7 Wh kg⁻¹). [42] And the photograph in the inset of Figure 7d shows two asymmetric supercapacitors in series can light up one LED indicators in red (1.5 V) after being charged to 3 V in 8 s at the current density of 20 A g⁻¹, demonstrating the supercapacitors can be used as efficient power sources for practical applications.

4. Conclusion

The nitrogen-doped porous carbon is prepared by white clovers and the activating agent ZnCl₂. Owing to high BET specific surface areas (857.0 m² g⁻¹) and superior surface functionalities (6.9 wt% nitrogen content), WCC-2 has high specific capacitance (233.1 F g⁻¹ at the current density of 1 A g⁻¹), possesses good capacitance

retention capability and an excellent cycling stability. Besides the inherent advantages, the WCC-2//WCC-2 symmetric supercapacitor device delivers a high energy density of 30 W h kg^{-1} at the power density of 503.5 W kg^{-1} . Therefore, it is a promising strategy to employ biomaterial white clovers as advanced electrode materials for high-performance supercapacitors.

Acknowledgment

This research was financially supported by the National Science Foundation of China (NO.21164009, 21174114), the program for Changjiang Scholars and Innovative Research Team in University (IRT1177), the Science and Technology Program of Gansu Province (NO.1308RJZA295, 1308RJZA265), Key Laboratory of Eco-Environment-Related Polymer Materials (Northwest Normal University) of Ministry of Education, and Key Laboratory of Polymer Materials of Gansu Province.

References

- 1 Y. Z. Zhang, Y. Wang, T. Cheng, W. Y. Lai, H. Pang and W. Huang, *Chem. Soc. Rev.*, 2015, **44**, 5181-5199
- 2 X. Yang, C. Chen, Y. Wang, L. Qiu and D. Li, *Science*, 2013, **341**, 534-537.
- 3 E. Frackowiak and F. Beguin, *Carbon*, 2001, **39**, 937-950.
- 4 L. Dai, D. W. Chang, J. B. Baek and W. Lu, *Small*, 2012, **8**, 1130-1166.
- 5 H. J. Denisa, S. Mykola, Q. L. Gao and J. Teresa, *Adv. Funct. Mater.*, 2009, **19**, 438-447.
- 6 J. Chang, Z. Gao, X. Wang, D. Wu, F. Xu, X. Wang, Y. Guo and K. Jiang, *Electrochim. Acta*, 2015, **157**, 290-298.
- 7 L. F. Chen, X. D. Zhang, H. W. Liang, M. Kong, Q. F. Guan, P. Chen, Z. Y. Wu and S. H. Yu, *ACS Nano*, 2012, **6**, 7092-7102.
- 8 Y. Zhao, M. Liu, X. Deng, L. Miao, P. K. Tripathi, X. Ma, D. Zhu, Z. Xu, Z. Hao and L. Gan, *Electrochim.*

Acta, 2015, **153**, 448-455.;

9 D. Zhu, Y. Wang, L. Gan, M. Liu, K. Cheng, Y. Zhao, X. Deng and D. Sun, *Electrochim. Acta*, 2015, **158**, 166-174.

10 Y. Zhai, Y. Dou, D. Zhao, P. F. Fulvio, R. T. Mayes and S. Dai, *Adv. Mater.*, 2011, **23**, 4828-4850.

11 J. Tang, J. Liu, C. Li, Y. Li, M. O. Tade, S. Dai and Y. Yamauchi, *Angew. Chem. Int. Ed.*, 2015, **54**, 588-593.

12 R. Ramanathan and V. Bansal, *RSC Adv.*, 2015, **5**, 1424-1429.

13 W. Luo, B. Wang, C. G. Heron, M. J. Allen, J. Morre, C. S. Maier, W. F. Stickle and X. Ji, *Nano Lett.*, 2014, **14**, 2225-2229.

14 C. Hu, S. He, S. Jiang, S. Chen and H. Hou, *RSC Adv.*, 2015, **5**, 14441-14447.

15 S. Dutta, A. Bhaumik and K. C. W. Wu, *Energy Environ. Sci.*, 2014, **7**, 3574-3592.

16 S. Mascotto, D. Kuzmicz, D. Wallacher, M. Siebenbürger, D. Clemens, S. Risse, J. Yuan, M. Antonietti and M. Ballauff, *Carbon*, 2015, **82**, 425-435.

17 A. S. Pensado, F. Malberg, M. C. Gomes, A. A. Pádua, J. Fernández and B. Kirchner, *RSC Adv.*, 2014, **4**, 18017-18024.

18 Q. Wang, Q. Cao, X. Wang, B. Jing, H. Kuang and L. Zhou, *J. Power Sources*, 2013, **225**, 101-107.

19 J. Ding, H. Wang, Z. Li, K. Cui, D. Karpuzov, X. Tan, A. Kohandehghan and D. Mitlin, *Energy Environ. Sci.*, 2015, **8**, 941-955.

20 X. L. Wu, T. Wen, H. L. Guo, S. Yang, X. Wang and A. W. Xu, *ACS Nano*, 2013, **7**, 3589-3597.

21 I. Vaseva, Y. Akiskan, K. Demirevska, I. Anders and U. Feller, *Sci. Horticulture-Amsterdam*, 2011, **130**, 653-659.

22 N. M. Casey, D. Milbourne, S. Barth, M. Febrer, G. Jenkins, M. T. Abberton, C. Jones and D. Thorogood, *Theor. Appl. Genet.*, 2010, **121**, 567-576.

- 23 M. A. Lillo-Ródenas, D. Lozano-Castelló, D. Cazorla-Amorós and A. Linares-Solano, *Carbon*, 2001, **39**, 751-759.
- 24 X. Ma, M. Liu, L. Gan, Y. Zhao and L. Chen, *J. Solid State Electr.*, 2013, **17**, 2293-2301.
- 25 H. Zhong, C. Deng, Y. Qiu, L. Yao and H. Zhang, *J. Mater. Chem. A*, 2014, **2**, 17047-17057.
- 26 M. Liu, J. Qian, Y. Zhao, D. Zhu, L. Gan and L. Chen, *J. Mater. Chem. A*, 2014, **3**, 11517-11526.
- 27 P. K. Tripathi, M. Liu, Y. Zhao, X. Ma, L. Gan, O. Noonanb and C. Yu, *J. Mater. Chem. A*, 2014, **2**, 8534-8544.
- 28 J. P. Paraknowitsch, J. Zhang, D. S. Su, A. Thomas and M. Antonietti, *Adv. Mater.*, 2010, **22**, 87-93.
- 29 Z. Li, Z. Xu, X. Tan, H. Wang, C. M. B. Holt, T. Stephenson, B. C. Olsen and D. Mitlin, *Energ. Environ. Sci.*, 2013, **6**, 871-878.
- 30 J. R. Pels, F. Kapteijn, J. A. Moulijn, Q. Zhu and K. M. Thomas, *Carbon*, 1995, **33**, 1641-1653.
- 31 H. C. Chen, F. G. Sun, J. T. Wang, W. C. Li, W. M. Qiao, L. C. Ling and D. H. Long, *J. Phys. Chem. C*, 2013, **117**, 8318-8328.
- 32 S. Gao, K. Geng, H. Liu, X. Wei, M. Zhang, P. Wang and J. Wang, *Energ. Environ. Sci.*, 2015, **8**, 221-229.
- 33 A. Sadezky, H. Muckenhuber, H. Grothe, R. Niessner and U. Pöschl, *Carbon*, 2005, **43**, 1731-1742.
- 34 H. Wang, Z. Xu, A. Kohandehghan, Z. Li, K. Cui, X. Tan, T. J. Stephenson, C. K. King'onde, C. M. Holt, B. C. Olsen, J. K. Tak, D. Harfield, A. O. Anyia and D. Mitlin, *ACS Nano*, 2013, **7**, 5131-5141.
- 35 X. Wu, J. Zhou, W. Xing, G. Wang, H. Cui, S. Zhuo, Q. Xue, Z. Yana and S. Z. Qiao, *J. Mater. Chem.*, 2012, **22**, 23186-23193.
- 36 D. Puthusseri, V. Aravindan, S. Madhavi and S. Ogale, *Energ. Environ. Sci.*, 2014, **7**, 728-735.
- 37 H. Wu, X. Y. Wang, L. L. Jiang, C. Wu, Q. L. Zhao, X. Liu, B. A. Hu and L. H. Yi, *J. Power Sources*, 2013, **226**, 202-209.

- 38 L. Sun, C. Tian, Y. Fu, Y. Yang, J. Yin, L. Wang and H. Fu, *Chem-Eur. J.*, 2014, **20**, 564-574.
- 39 Q. Wang, J. Yan, Y. Wang, T. Wei, M. Zhang, X. Jing and Z. Fan, *Carbon*, 2014, **67**, 119-127.
- 40 J. Yan, Q. Wang, C. Lin, T. Wei and Z. Fan, *Adv. Energy Mater.*, 2014, **4**, 201400500.
- 41 W. H. Qu, Y. Y. Xu, A. H. Lu, X. Q. Zhang and W. C. Li, *Bioresource Technol.*, 2015, **189**, 285-291.
- 42 Q. Zhao, X. Wang, H. Xia, J. Liu, H. Wang, J. Gao, Y. Zhang, J. Liu, H. Zhou, X. Li, S. Zhang and X. Wang, *Electrochim. Acta*. 2015, **173**, 566-574

Figure captions:

Figure 1. FE-SEM images of: (a) the raw material of white clovers after grinding and carbons prepared with different addition of activating agent: (b) WCC-0; (c) WCC-1; (d) WCC-2 and (e) WCC-3 samples

Figure 2. (a) Low and (b) high magnification high-resolution TEM images of WCC-2

Figure 3. (a) Nitrogen adsorption-desorption isotherms, (b) and inset (b) pore size distributions of the as-prepared carbons

Figure 4. (a) XPS survey spectra, (b) High-resolution XPS spectra of the deconvoluted N 1s peak and (c) Element mapping images (selected from the square region) of WCC-2

Figure 5. (a) XRD patterns and (b) Raman spectrum of WCC-2

Figure 6. (a) CV curves at a scan rate of 50 mVs^{-1} and (b) GCD curves at the current density of 1 A g^{-1} for all as-prepared carbons; (c) CV curves with various scan rates, (d) GCD curves at different current densities, (e) the change of specific capacitance with the increase of current density, (f) EIS and (g) Cycling performances at the current density of 5 A g^{-1} of WCC-2 and the inset is GC curves of the first three and the last three cycles, respectively.

Figure 7. Electrochemical characteristics of WCC-2//WCC-2 symmetric supercapacitor in $0.5 \text{ M Na}_2\text{SO}_4$ aqueous electrolyte in a two electrode system: (a) CV curves in different voltage windows at 50 mV s^{-1} . (b) CV curves in 2.0 V at different scan rates. (c) Galvanostatic charge/discharge curves at different current densities. (d) The Ragone plots of the symmetric supercapacitor

Table 1. Elemental analysis, BET surface area, and pore structure characterization parameters of the as-prepared carbons

a) Specific surface area determined according to BET (Brunauer-Emmett-Teller) method. b) Micropore surface area from t-plot method. c) Adsorption average pore diameter. d) Total pore volume.

Figure 1

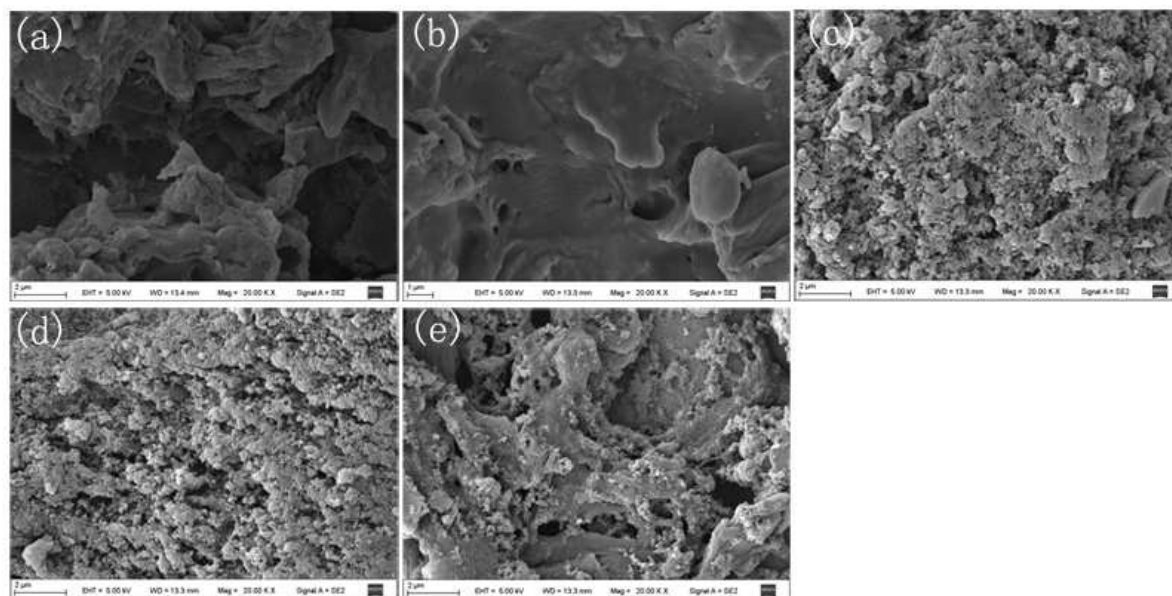


Figure 2

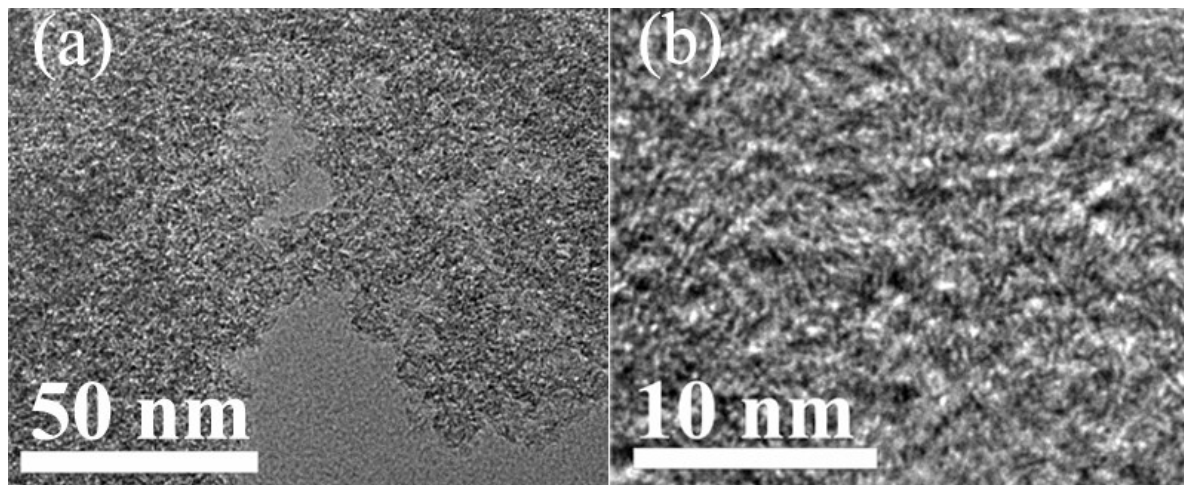


Figure 3

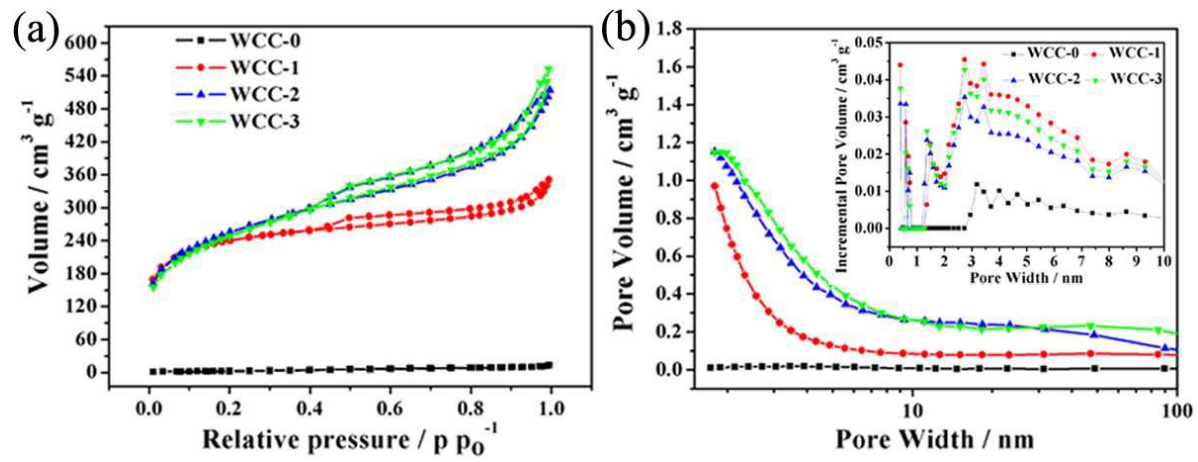


Figure 4

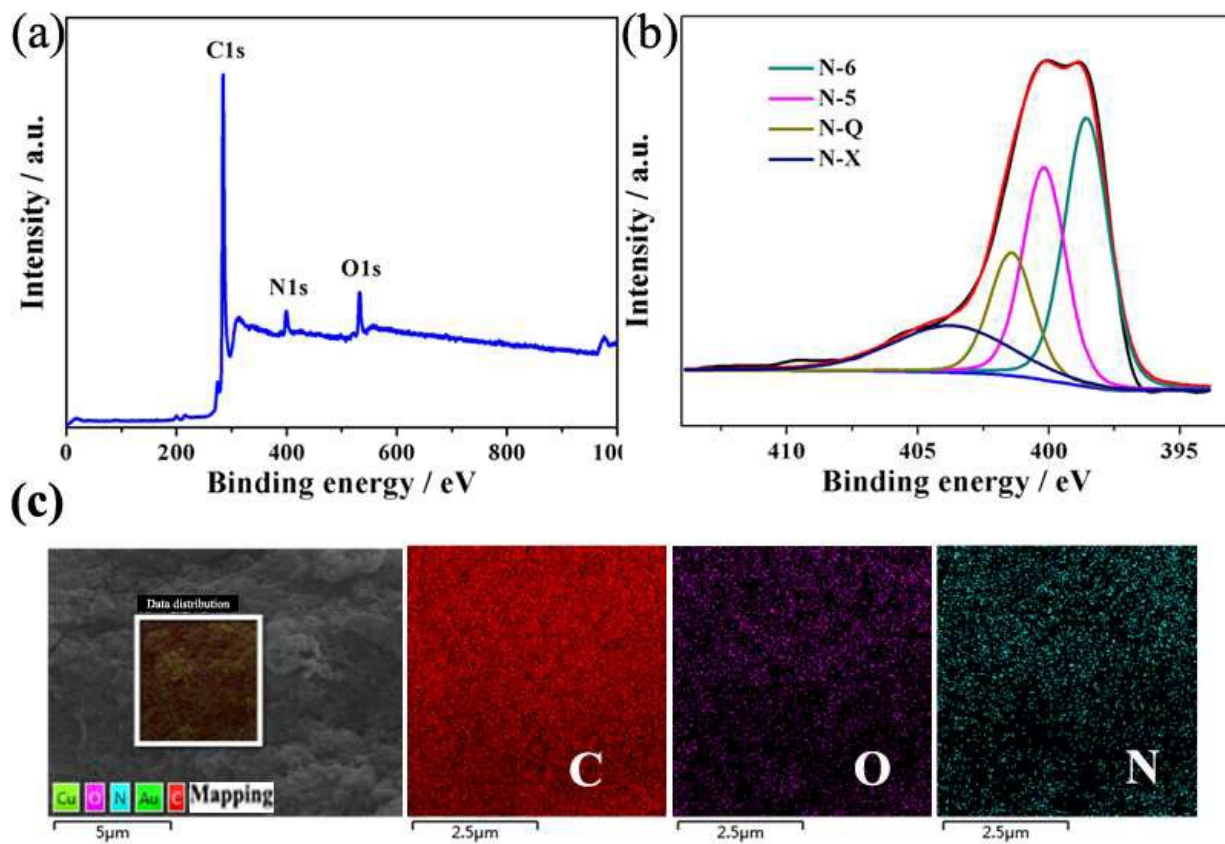


Figure 5

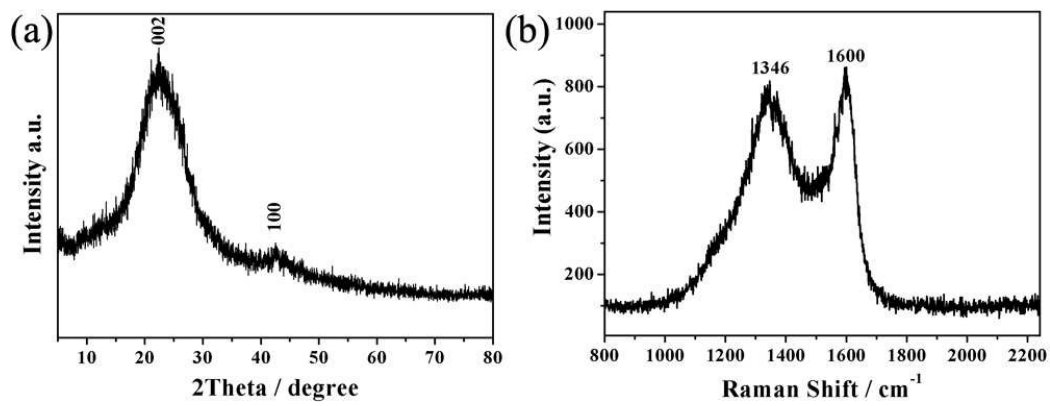


Figure 6

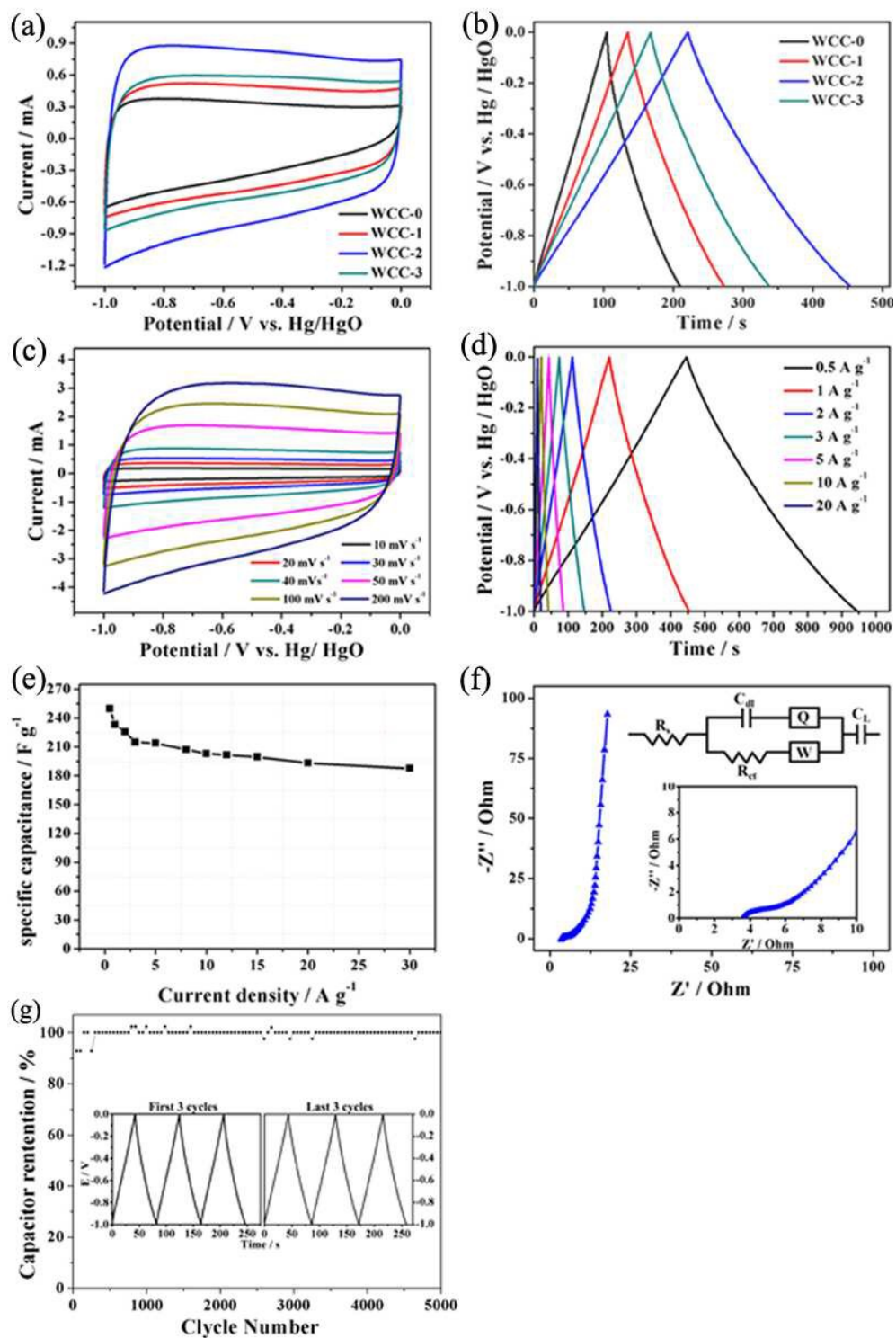


Figure 7

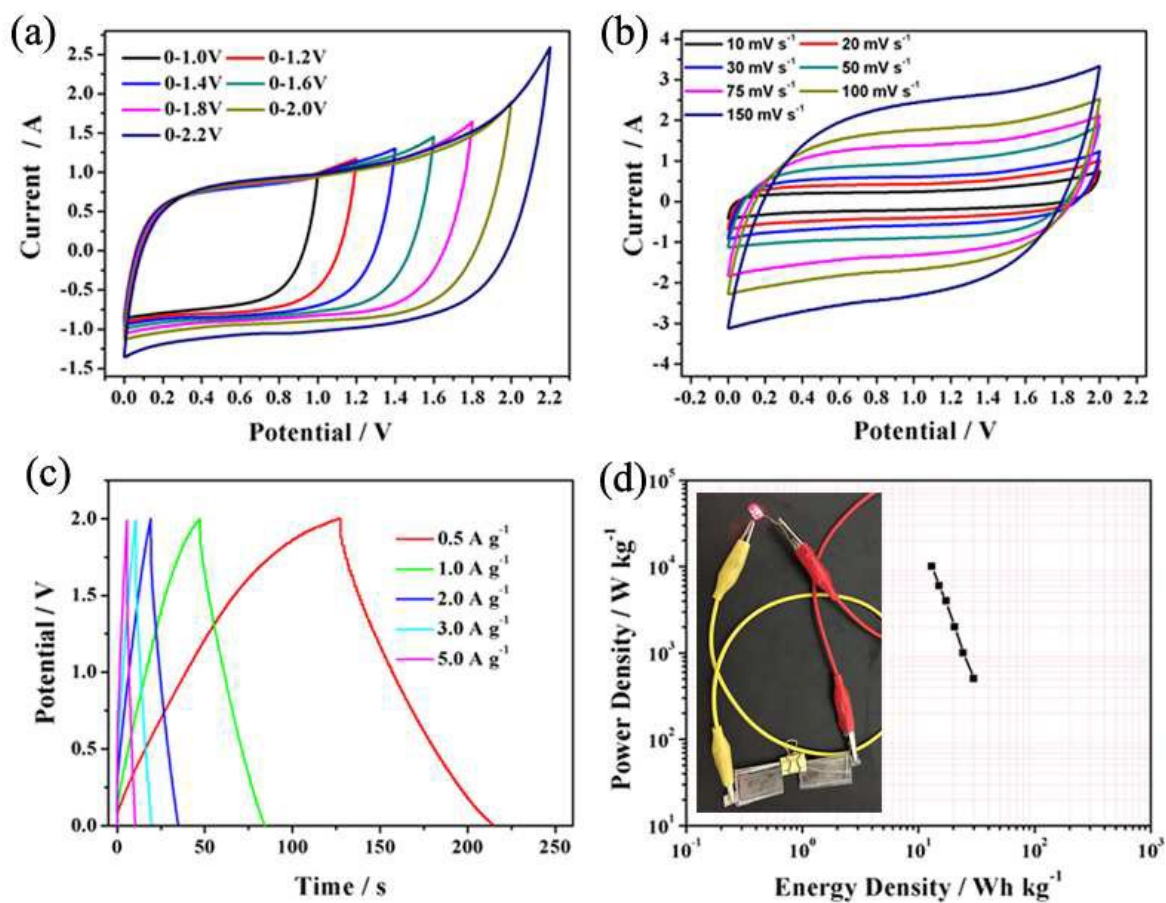
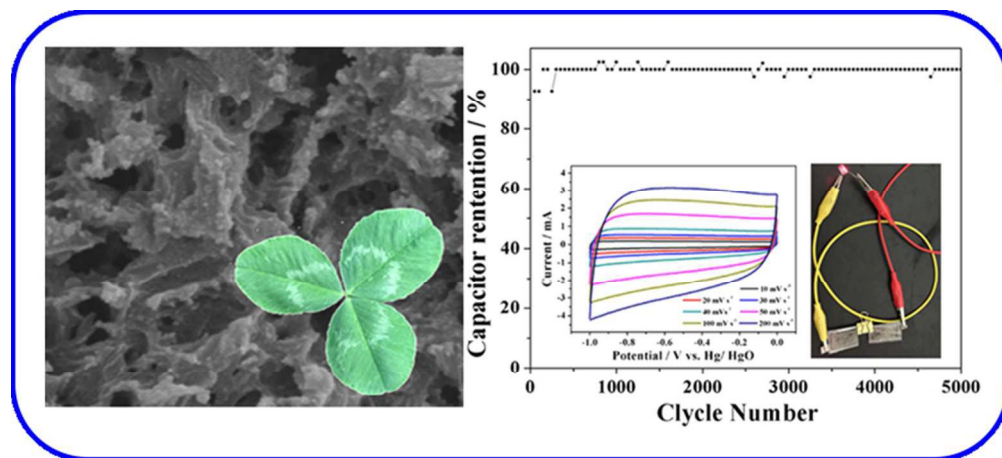


Table 1

Samples	Elemental analysis			$S_{\text{BET}}^{\text{a}}$ ($\text{m}^2 \text{g}^{-1}$)	$S_{\text{mic}}^{\text{b}}$ ($\text{m}^2 \text{g}^{-1}$)	D^{c} (nm)	$V_{\text{total}}^{\text{d}}$ ($\text{cm}^3 \text{g}^{-1}$)
	C %	N %	H %				
WCC-0	59.3	4.1	1.3	12.9	0	0	0.02
WCC-1	77.1	6.8	1.7	763.1	353.4	2.84	0.54
WCC-2	78.3	6.9	1.6	857.0	194.6	3.71	0.80
WCC-3	79.4	6.8	1.6	851.0	121.3	4.02	0.85



223x101mm (96 x 96 DPI)